JOURNAL OF GEOPHYSICAL RESEARCH, VOL. 111, B12401, doi:10.1029/2005JB004101, 2006



# Shear-enhanced compaction and strain localization: Inelastic deformation and constitutive modeling of four porous sandstones

Patrick Baud,[1] Veronika Vajdova,[2,3] and Teng-fong Wong[2]

Received 11 October 2005; revised 21 May 2006; accepted 17 August 2006; published 7 December 2006.

[1] We studied the mechanics of compactant failure in four sandstones associated with a broad range of failure modes in the brittle-ductile transition. While Berea and Bentheim sandstones can fail by compaction localization, homogeneous cataclastic flow dominates failure modes in Adamswiller and Darley Dale sandstones at high effective pressures. We acquired new experimental data to complement previous studies, focusing on the strain hardening behavior in samples under drained conditions. The initial yield stresses were identified as the critical stresses at the onset of shear-enhanced compaction, subsequent yield stresses were considered to depend on hardening given by plastic volumetric strain. The yield stresses were described by elliptical yield caps in the stress space, and we compared the cap evolution with two constitutive models: the critical state model and the cap model. Bentheim sandstone showed the best agreement with both models to relatively large strains. Darley Dale sandstone showed the best agreement with the associated flow rule as prescribed by the normality condition, which is implicitly assumed in both constitutive models. Shear-enhanced compaction in Bentheim and Berea sandstones was appreciably more than that predicted for an associative flow rule, with the implication that a nonassociative model is necessary for capturing the inelastic and failure behavior of these sandstones over a broad range of effective pressures. With reference to the nonassociative model formulated by Rudnicki and Rice, bifurcation analysis would predict the transition of failure mode from shear band to compaction band and ultimately to cataclastic flow, in qualitative agreement with the experimental observations.

**Citation:** Baud, P., V. Vajdova, and T. Wong (2006), Shear-enhanced compaction and strain localization: Inelastic deformation and constitutive modeling of four porous sandstones, *J. Geophys. Res.*, *111*, B12401, doi:10.1029/2005JB004101.

## 1. Introduction

[2] In response to an applied stress field or pore pressure change, the pore space of a rock may dilate or compact. Such porosity change arises from the interplay of several micromechanical processes, including microcracking, grain crushing and pore collapse. Rock mechanics studies have demonstrated that in the brittle-ductile transition dilatant and compactant failures are associated with several distinct failure modes. The mode of dilatant failure can be either axial splitting or shear faulting, which arises from the nucleation, propagation and coalescence of stress-induced cracks [*Paterson and Wong*, 2005]. In contrast, compactant failure typically occurs in porous rocks under relatively high confinement, with a failure mode conventionally described as homogeneous cataclastic flow [*Handin et al.*, 1963; *Menéndez et al.*, 1996].

[3] In a previous study, *Wong et al.* [1997] investigated this transition from brittle faulting to cataclastic flow in six sandstones with porosities ranging from 15% to 35%. By systematically characterizing the inelastic behavior and acoustic emission activity associated with these two failure modes, they showed that the failure envelopes for the brittle strength and compactive yield stress are sensitively dependent on microstructural parameters such as porosity and grain size. The comprehensive database provides a useful framework for the analysis of the two end-members of dilatant and compactive failure, and it has motivated the formulation of several constitutive models [e.g., *Issen*, 2002; *Ricard and Bercovici*, 2003; *Hamiel et al.*, 2004; *Grueschow and Rudnicki*, 2005] which attempt to capture the key mechanical attributes and failure modes.

[4] Nevertheless there are at least two fundamental issues on the mechanics of compactant failure that were not adequately addressed in this previous study. First, while their data on initial yield stresses of porous sandstones are in qualitative agreement with constitutive models such as the critical state [*Schofield and Wroth*, 1968] and cap [*DiMaggio and Sandler*, 1971] models, *Wong et al.* [1997] did not compare their data quantitatively with specific predictions of such models on the strain hardening behavior and

[1] Institut de Physique du Globe, CNRS, Université Louis Pasteur, Strasbourg, France.
[2] Department of Geosciences, State University of New York at Stony Brook, Stony Brook, New York, USA.
[3] Now at ReedHycalog, Houston, Texas, USA.


0148-0227/06/2005JB004101$09.00

**Table 1.** Petrophysical Description of the Four Sandstones Investigated in This Study

| Sandstone | Porosity,% | Grain Radius, mm | Composition | Reference |
|---|---|---|---|---|
| Darley Dale | 13 | 0.17 | quartz: 66%, feldspar 21%, mica 3%, clay ~6% | *Wong et al.* [1997] |
| Berea | 21 | 0.13 | quartz: 75%, feldspar 10%, carbonate 5%, clay ~10% | *Zhang et al.* [1990a] |
| Adamswiller | 22.6 | 0.09 | quartz: 71%, feldspar 9%, oxides and mica 5%, clay ~11% | *Wong et al.* [1997] |
| Bentheim | 22.8 | 0.105 | quartz: 95%, 3% kaolinite, 2% orthoclase | *Klein et al.* [2001] |

evolution of subsequent yield surfaces. Such a comparison is important since the development of physically realistic constitutive models for inelastic compaction and failure in porous rocks is critical to many geological and geotechnical applications that depend on the ability to predict the development of porosity loss, dewatering and pore pressure excess in tectonic settings such as accretionary prisms and fault zones [*Byrne et al.*, 1993; *Byerlee*, 1990; *Sibson*, 1994], as well as the occurrence and extent of subsidence and well failure in reservoirs and aquifers [*Nagel*, 2001; *Fredrich and Fossum*, 2002].

[5] Second, by focusing on homogeneous cataclastic flow as the dominant end-member for compactant failure the assumption is implicitly made that strain localization would not develop while a porous rock undergoes compaction. However, recent geologic [*Mollema and Antonellini*, 1996; *Sternlof et al.*, 2004] and laboratory [*Olsson and Holcomb*, 2000; *DiGiovanni et al.*, 2000] studies in porous sandstones have documented the pervasive occurrence of localized failure during compaction. Such localized compactant failure is often associated with stress states in the transitional regime between brittle faulting and cataclastic flow [*Klein et al.*, 2001], manifested by structures showing a broad spectrum of geometric complexity and distinct acoustic emission activity [*Baud et al.*, 2004]. Significant reduction of permeability has also been observed in samples undergoing compaction localization [*Holcomb and Olsson*, 2003; *Vajdova et al.*, 2004a]. Since strain localization as a failure mode can significantly influence the stress field, strain partitioning and fluid transport in many tectonic settings, it is of fundamental importance to have a physical understanding of such compaction localization phenomena and their relation to the constitutive behavior.

[6] This study was undertaken to investigate a number of questions related to these two issues. To what extent are the mechanical data in agreement with constitutive model predictions on the evolution of yield stresses with strain hardening? What are the mechanical attributes that promote the development of strain localization in the transitional regime between the end-members of compactive cataclastic flow and brittle faulting? Theoretical analysis of strain localization shows that its onset is sensitive to whether the normality condition applies and the inelastic behavior can be described by an associated flow rule [*Issen and Rudnicki*, 2000]. It is often assumed in constitutive models that cataclastic flow can be described as associative, and indeed the mechanical data seem to indicate that the normality condition applies [*Wong et al.*, 1997; *Wong and Baud*, 1999]. Does normality also apply to the constitutive behavior associated with compaction localization in the transitional regime?

[7] Four sandstones, Adamswiller, Bentheim, Berea and Darley Dale, were selected because of the broad range of failure modes observed in these rocks in relation to the brittle-ductile transition [*Baud et al.*, 2004]. While mechanical data for Darley Dale, Adamswiller and Berea sandstones in the cataclastic flow regime are available from previous studies, we conducted here additional experiments focusing on the transitional regime. Among the four, compaction localization in Bentheim sandstone was observed to develop over the broadest range of pressure. Previous studies [*Wong et al.*, 2001; *Baud et al.*, 2004] on the Bentheim sandstone were conducted mostly on nominally dry samples. Here we present a comprehensive series of experiments on saturated Bentheim sandstone samples, and collectively the data provide useful insights into the development of cataclastic flow and compaction localization in water-saturated sandstones.

## 2. Mechanical Deformation and Failure Mode

[8] Petrophysical descriptions of the four sandstones are compiled in Table 1. While their average grains sizes are comparable, the porosities of the four range from 13% to 23% and there are significant contrasts in the modal compositions. The Darley Dale and Berea sandstone samples were cored from the same blocks used by *Baud et al.* [2000a, 2004]. Bentheim sandstone samples were from a new block considered to be similar to that previously studied by *Baud et al.* [2004] and *Vajdova et al.* [2004a]. These samples were cored perpendicular to the bedding in the three sandstones. In contrast the Adamswiller sandstone samples were cored parallel to the bedding, from the same block studied by *Wong et al.* [1997].

[9] In this paper we will use the convention that the compressive stresses and compactive strains (i.e., shortening and porosity decrease) are considered to be positive. We will denote the maximum and minimum (compressive) principal stresses by $\sigma_1$ and $\sigma_3$, respectively. The pore pressure will be denoted by $P_p$, and the difference $P_c - P_p$ between the confining pressure ($P_c = \sigma_2 = \sigma_3$) and pore pressure will be referred to as the "effective pressure" $P_{eff}$. The effective mean stress $(\sigma_1 + 2\sigma_3)/3 - P_p$ will be denoted by $P$ and the differential stress $\sigma_1 - \sigma_3$ by $Q$.

### 2.1. Experimental Procedure

[10] The samples were ground to a cylindrical shape with diameter of 18.4 mm and length 38.1 mm. They were jacketed with polyolefine tubing, saturated with distilled water and deformed under fully drained conditions at a fixed pore pressure of 10 MPa. Kerosene was used as the confining medium. Both confining pressure and pore pressure were monitored by strain gage pressure transducers to accuracies of 0.5 and 0.125 MPa, respectively. Adjustment of a pressure generator kept the pore pressure constant, and the pore volume change was recorded by monitoring the piston displacement of the pressure generator with a displacement transducer (DCDT). The porosity change was

calculated from the ratio of the pore volume change to the initial bulk volume of the sample. The axial load was measured with an external load cell with an accuracy of 1 kN. The displacement was measured outside the pressure vessel with a DCDT mounted between the moving piston and the fixed upper platen. The uncertainty of the axial displacement measurement was 10 $\mu$m. The machine stiffness was 238 kN/mm.

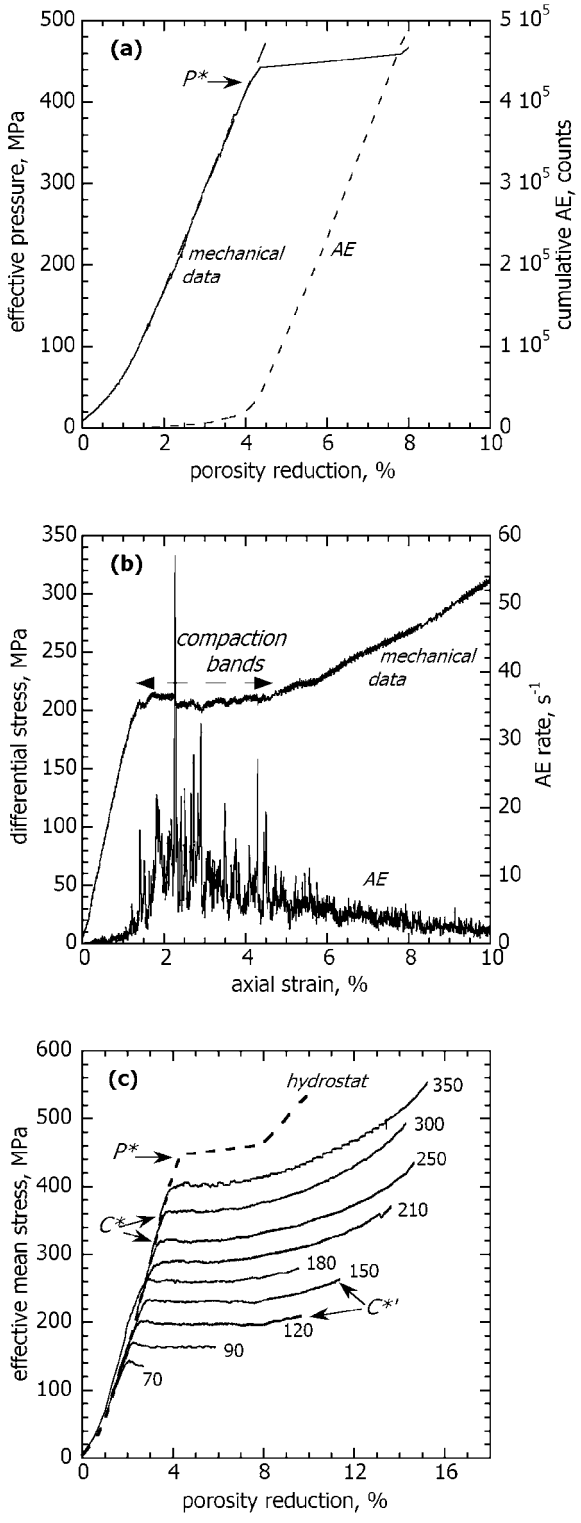


[11] The sandstone samples were deformed in the conventional triaxial configuration at a nominal axial strain rate of $1.3 \times 10^{-5}$ s$^{-1}$ at room temperature and under confining pressures ranging from 40 to 350 MPa, following the methodology of *Wong et al.* [1997]. To record acoustic emission (AE) activity during triaxial experiments, we used a piezoelectric transducer mounted on the spacer attached to the jacketed sample. The AE signals were conditioned by a preamplifier (gain 40dB, frequency response 1.5 kHz to 5 MHz). To distinguish AE events from electric noise, a discriminator was used to check the amplitude and oscillational characteristics of the incoming signal. (See *Zhang et al.* [1990b] for details.)

### 2.2. Bentheim Sandstone: Mechanical Data, AE Activity, and Failure Mode

[12] We will first present our new data on saturated Bentheim sandstone samples, comparing them with previous data on nominally dry samples [*Wong et al.*, 2001; *Baud et al.*, 2004]. The porosity reduction of Bentheim sandstone under hydrostatic loading is presented in Figure 1a. Typically the hydrostat of a porous sandstone shows (1) an initial nonlinear stage at low effective pressure, corresponding to the closure of crack porosity (inferred to be $\sim$0.4% for Bentheim sandstone); (2) an approximately linear poroelastic stage; and (3) a third stage showing significant deviation from poroelasticity, corresponding to the onset of grain crushing and pore collapse [*Zhang et al.*, 1990a]. The effective pressure at the transition from the second to third stage is denoted by $P^*$, which corresponds to an inflection point in the hydrostat and an upsurge in AE activity. The critical effective pressure $P^*$ for saturated Bentheim sandstone was observed to be 420 MPa, and taking into consideration its porosity ($\phi$) and grain radius ($R$) this value follows the trend for $P^* \propto (\phi R)^{-3/2}$ as deduced by *Zhang et al.* [1990a] and *Wong et al.* [1997]. In stage 3 grain crushing and pore collapse resulted in a dramatic porosity decrease of $\sim$3% while the effective pressure increased by a relatively small increment from 452 MPa to 477 MPa.

[13] Figure 1b shows the axial stress-strain curve for a sample deformed at 250 MPa of effective pressure. After

**Figure 1.** Mechanical data for saturated Bentheim sandstone. (a). Effective pressure and cumulative count of acoustic emission (AE) as functions of porosity reduction in a hydrostatic experiment. Arrow indicates the critical pressure $P^*$ for the onset of pore collapse. Dashed linear regression line denotes the linear part of the hydrostat used for the calculation of pore compressibility. (b) Differential stress and acoustic emission rate as functions of axial strain in a triaxial experiment at effective pressure of 250 MPa. The range of axial strain at which microstructural observations indicate the development of discrete compaction bands is marked on the figure. (c) Effective mean stress as a function of porosity reduction for triaxial compression experiments at effective pressures indicated by numbers (in MPa) next to each curve. For reference the hydrostatic data are shown as the dashed line. Arrows mark critical stress states $C^*$ and $C^{*\prime}$ for selected experiments and the critical pressure $P^*$ for the hydrostatic experiment.

**Table 2.** Mechanical Data of the Samples Investigated in This Study

| | $C^*$ | | $C^{*\prime}$ | | |
|---|---|---|---|---|---|
| Effective Pressure $\sigma_3 - P_p$, MPa | Effective Mean stress $P$, MPa | Differential Stress $Q$, MPa | Effective Mean stress $P$, MPa | Differential Stress $Q$, MPa | Comments |
| | | | *Darley Dale* | | |
| 80 | 164 | 251 | - | - | high-angle shear bands |
| 90 | 178 | 264 | - | - | high-angle shear bands |
| 95 | 186 | 269 | - | - | high-angle shear bands |
| 100 | 188 | 269 | - | - | homogeneous cataclastic flow |
| 110 | 200 | 270 | | | homogeneous cataclastic flow |
| 150 | 242 | 274 | 272 | 363 | homogeneous cataclastic flow |
| 180 | 267 | 260 | 317 | 408 | homogeneous cataclastic flow |
| 200 | 285 | 253 | 417 | 530 | homogeneous cataclastic flow |
| 240 | 315 | 222 | - | - | homogeneous cataclastic flow |
| 300 | 357 | 171 | - | - | homogeneous cataclastic flow |
| $P^*$ | 380 | 0 | - | - | |
| | | | *Berea* | | |
| 40 | 98 | 172 | - | - | high-angle shear bands |
| 50 | 111 | 182 | - | - | high-angle shear bands |
| 60 | 120 | 179 | - | - | high-angle shear bands |
| 75 | 137 | 184 | - | - | high-angle shear bands |
| 90 | 154 | 190 | - | - | high-angle shear bands |
| 100 | 165 | 195 | - | - | diffuse compaction bands |
| 150 | 214 | 191 | - | - | discrete and diffuse compaction bands |
| 200 | 260 | 178 | - | - | homogeneous cataclastic flow |
| 250 | 301 | 151 | - | - | homogeneous cataclastic flow |
| 300 | 341 | 122 | - | - | homogeneous cataclastic flow |
| $P^*$ | 400 | 0 | - | - | |
| | | | *Adamswiller* | | |
| 40 | 77 | 115 | - | - | high-angle shear bands |
| 60 | 101 | 123 | - | - | - |
| 100 | 138 | 114 | - | - | - |
| 150 | 176 | 78 | - | - | - |
| 175 | 193 | 54 | - | - | - |
| P* | 190 | 0 | - | - | - |
| | | | *Bentheim* | | |
| 50 | 111 | 181 | - | - | high-angle shear bands (45°) |
| 70 | 138 | 203 | - | - | high-angle shear bands (50°) |
| 90 | 165 | 224 | - | - | discrete compaction bands + high angle shear bands |
| 120 | 195 | 225 | 208 | 263 | discrete compaction bands |
| 150 | 227 | 228 | 263 | 337 | discrete compaction bands |
| 180 | 253 | 216 | 370 | 477 | discrete compaction bands |
| 210 | 280 | 210 | 435 | 553 | discrete compaction bands |
| 250 | 314 | 193 | - | - | discrete compaction bands |
| 300 | 358 | 170 | - | - | discrete compaction bands |
| 350 | 394 | 129 | - | - | discrete compaction bands |
| $P^*$ | 420 | 0 | - | - | |

attaining an initial peak the differential stress remained relatively flat and only after an axial strain of ~5% had accumulated was strain hardening appreciable. However, it should be noted that the differential stress was not exactly constant on the plateau, but instead was punctuated by episodic stress drops accompanied by upsurges in AE activity. According to our microstructural analysis the failure mode associated with such a plateau typically involves the development of discrete compaction bands. These are relatively narrow tabular structures (with widths comparable to the grain size) oriented subperpendicular to $\sigma_1$ [*Baud et al.*, 2004]. The number of compaction bands increases linearly with cumulative axial strain [*Vajdova et al.*, 2004a], and when most of the sample volume was covered with such discrete bands, the stiffer rock started to harden and the AE activity decayed slowly and continuously (Figure 1b). The inelastic behavior and failure mode observed in our saturated samples are qualitatively similar to those of nominally dry samples reported by *Wong et al.* [2001] and *Baud et al.* [2004]. Our observations indicate that localized failure developed by discrete compaction bands at the very broad range of effective pressures between 120 and 350 MPa. The failure mode switched to high-angle shear bands at effective pressures between 50 and 90 MPa (Table 2).

[14] Figure 1c compiles our new mechanical data for saturated Bentheim sandstone at effective pressures between 50 and 350 MPa. In this pressure range, dilatancy was not observed and to underscore the influence of nonhydrostatic loading on the inelastic yield behavior we plot here the effective mean stress as a function of porosity change. The nonhydrostatic and hydrostatic loadings are coupled in our

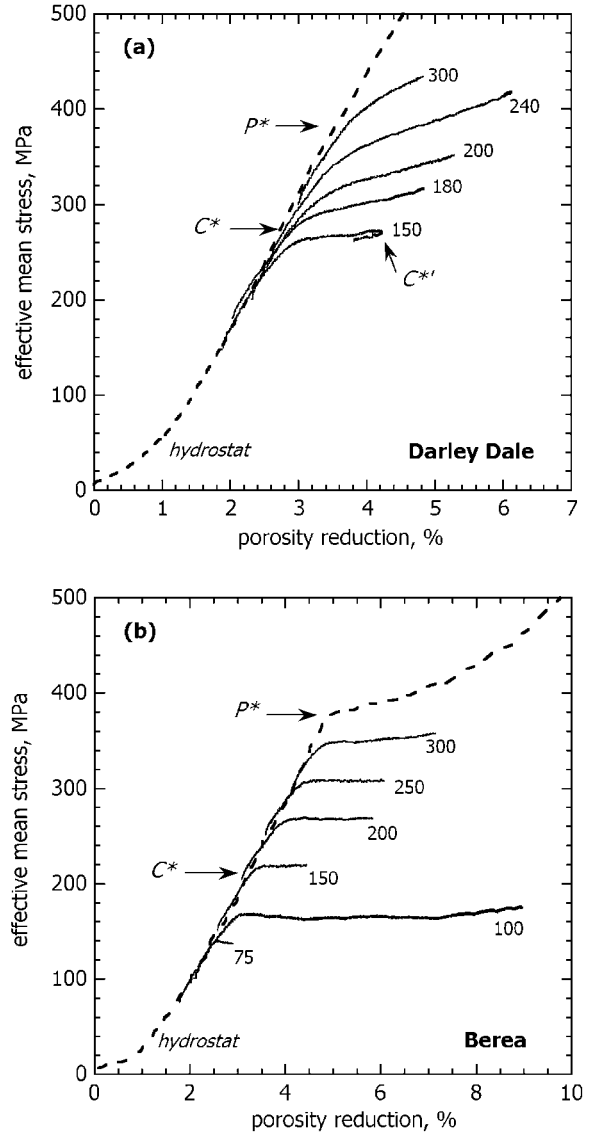


**Figure 2.** Effective mean stress versus porosity reduction for triaxial compression experiments on (a) Darley Dale and (b) Berea sandstone. The effective pressures are indicated by numbers (in MPa) next to each curve. For reference the hydrostatic data are shown as the dashed lines. Arrows mark critical stress states $P^*$ for hydrostatic experiments and $C^*$ and $C^{*\prime}$ for selected triaxial experiments.

conventional triaxial experiments. If the axial stress increases by an increment $\Delta\sigma_1$ while the confining and pore pressures are maintained constant, not only does the differential stress $Q$ increase by the amount $\Delta\sigma_1$ but the effective mean stress $P$ would also increase by $\Delta\sigma_1/3$. For elastic deformation the porosity change is solely controlled by the hydrostatic stresses and independent of the differential stress, and therefore the triaxial data (solid curves) in Figure 1c should coincide with the hydrostat (dashed curve). Any deviation from the hydrostat would imply that the porosity change in a triaxial compression experiment depends on not only the effective mean stress, but also the deviatoric stresses due to inelastic deformation. In all the experiments shown in Figure 1c the triaxial curve for a given effective pressure coincided with the hydrostat up to a critical stress state (indicated by $C^*$), beyond which there was an accelerated decrease in porosity in comparison to the hydrostat. At stress levels beyond $C^*$ the deviatoric stress field provided an inelastic contribution to the compactive strain, and this phenomenon of "shear-enhanced compaction" [*Wong et al.*, 1997] is attributed to the inception of grain crushing and pore collapse in the sandstone [*Menéndez et al.*, 1996; *Wu et al.*, 2000].

[15] The critical stress state $C^*$ for the onset of shear-enhanced compaction also marks the initial yield stress, which decreases with increasing effective pressure (Table 2). For the experiments at effective pressures between 90 MPa and 350 MPa, the stress levels initially stayed relatively constant beyond the initial yield point $C^*$, and as noted above these stress "plateaus" were punctuated by episodic stress drops manifested by upsurges in AE activity. After the porosity had been reduced inelastically by 5% or so, strain hardening was observed and further compaction would require appreciable increase of stress. Ultimately the sample attained the transitional point at which further increase of differential stress would induce the pore space to dilate rather than compact. Following *Baud et al.* [2000b], this critical stress state is denoted by $C^{*\prime}$ (Figure 1c). In selected experiments we deformed the samples to sufficiently high strain so that this transition from shear-enhanced compaction to dilatancy could be observed. The $C^{*\prime}$ data from these tests are compiled in Table 2.

### 2.3. Adamswiller, Darley Dale, and Berea Sandstones

[16] Representative stress-strain curves for Adamswiller, Darley Dale and Berea sandstones were presented by *Wong et al.* [1997], *Baud et al.* [2000a], and *Baud et al.* [2004]. Additional experiments were performed in this study to relatively large strains so the transitional points $C^{*\prime}$ can be determined. Curves for the effective stress as a function of porosity change in selected experiments for the Darley Dale and Berea sandstones are shown in Figure 2. The behavior of Darley Dale sandstone is different from Bentheim sandstone in two aspects. First, appreciable strain hardening was observed in Darley Dale sandstone without any plateaus in the stress level beyond the onset of shear-enhanced compaction. Second, episodic stress drops were not observed in Darley Dale sandstone during strain hardening (Figure 2a). A synopsis of the failure modes is included in Table 2. Microstructural observations show homogeneous cataclasis in samples deformed at effective pressures over 95 MPa, as described in detail by *Wu et al.* [2000]. Between 80 MPa and 95 MPa, conjugate shears at high angle were observed [*Baud et al.*, 2004].

[17] The behavior of Berea sandstone is similar to that of Bentheim sandstone in that beyond $C^*$ the stress levels initially remained relatively constant. However, episodic stress drops were not observed and in this respect its behavior is similar to Darley Dale sandstone (Figure 2b). At effective pressures between 50 and 90 MPa, high-angle shear bands comparable to those in Darley Dale sandstone were observed. Microstructural observations show that at intermediate effective pressures (90–200 MPa) a diffuse mosaic of compaction bands had developed in the samples [*Baud et al.*, 2004]. In samples failed at effective pressures above 250 MPa *Menéndez et al.* [1996] observed homoge-

neous cataclasis, but in light of recent observations of *Baud et al.* [2004] it is possible that part of the damage in these high-pressure samples may have been localized in diffuse bands.

[18] For Adamswiller sandstone, we conducted only one additional test at 175 MPa effective pressure to complement existing data from *Wong et al.* [1997]. The failure mode of this rock was not studied in detail. Overall the mechanical data of Adamswiller and Darley Dale sandstone are qualitatively similar, with significant strain hardening observed in both rocks at relatively high effective pressures. We did not conduct detailed microstructural observations on failed Adamswiller sandstone samples, but judging from exterior features of the failed sample and the continuous accumulation of AE recorded in all samples deformed beyond 40 MPa of effective pressure, as well as microstructural observations on sandstones of comparable porosity cored parallel to bedding [*Baud et al.*, 2004, 2005], we infer that the dominant failure mode for this rock was homogenous cataclastic flow.

## 3. Constitutive Models

[19] Plasticity theory provides a constitutive framework for the analysis of inelastic yield and compaction in a granular material such as soil [*Chen*, 1984; *Desai and Siriwardane*, 1984; *Davis and Selvadurai*, 2002], porous sandstone [*Wong et al.*, 1997; *Guéguen et al.*, 2004; *Grueschow and Rudnicki*, 2005], diatomites [*Fossum and Fredrich*, 2000], and carbonate rocks [*Vajdova et al.*, 2004b]. In particular, two classes of plasticity models are often invoked: the critical state model [*Schofield and Wroth*, 1968] which has had a profound impact in soil mechanics, and the cap model which was formulated by *DiMaggio and Sandler* [1971] with both soil and porous rock in mind. While many versions of the critical state model have been proposed [*Wood*, 1990], we will here focus on one proposed by *Carroll* [1991] for porous reservoir rocks. *Carroll*'s [1991] critical state model and *DiMaggio and Sandler*'s [1971] cap model have four common features. (1) They both assume the plastic yield behavior of the compactant rock is isotropic. (2) The yield function is assumed to be independent of the third stress invariant. (3) The strain hardening behavior is characterized by a yield function that depends solely on the plastic volumetric strain. (4) Both models assume the plastic flow to be associative satisfying the normality condition. We will briefly review these characteristics of the critical state and cap models before comparing them with our mechanical data.

### 3.1. Elliptic Yield Caps in Plasticity Models

[20] The first step in developing a plasticity model is to identify an appropriate yield function $f$ in the stress ($\sigma_{ij}$) space. If the yield behavior is isotropic, then the yield behavior can be described by a function dependent only on the three stress invariants, and furthermore if the yield behavior can be considered to be independent of the third stress invariant, then $f$ is a function of only the first and second stress invariants,

$$I_1 = (\sigma_{11} - P_p) + (\sigma_{22} - P_p) + (\sigma_{33} - P_p) \tag{1a}$$

$$J_2 = \left[(\sigma_{11} - \sigma_{22})^2 + (\sigma_{22} - \sigma_{33})^2 + (\sigma_{33} - \sigma_{11})^2\right] \Big/ 6 + \sigma_{12}^2 + \sigma_{23}^2 + \sigma_{13}^2 \tag{1b}$$

The constitutive models to be considered here all adopt a yield function of the form

$$f(\sigma_{ij}) = \frac{(I_1 - c)^2}{a^2} + \frac{J_2}{b^2} - 1 = 0 \tag{2}$$

which corresponds to an ellipse centered at ($c$, 0) with major and minor semiaxes of $a$ and $b$. The three parameters for the ellipse can be evaluated from conventional triaxial tests on saturated samples by noting that under axisymmetric loading the first stress invariant is related to the effective mean stress $P$ by $I_1 = 3P$ and the second invariant to the differential stress $Q$ by $3J_2 = Q^2$. Accordingly the constitutive model prescribes the triaxial compression data on yield stress to fall on the ellipse with semiaxes $A = a/3$ and $B = \sqrt{3}b$ and center at ($C = c/3$, 0):

$$\frac{(P - C)^2}{A^2} + \frac{Q^2}{B^2} = 1 \tag{3a}$$

[21] The yield function $f$ (and therefore the three parameters $a$, $b$ and $c$) is assumed to depend only on the plastic volumetric strain $\varepsilon_v^p$ as the rock undergoes inelastic deformation and work hardening. The initial yield stresses corresponding to $C^*$ at the onset of shear-enhanced compaction map are expected to fall on the initial elliptical cap for $\varepsilon_v^p = 0$. We will use $A_o$, $B_o$ and $C_o$ to denote the semiaxes and center of this initial cap.

[22] It should be noted that there are constitutive models that adopt caps that are nonelliptical. Indeed in critical state soil mechanics the yield function $Q + MP(\ln(P/P_{cr} - 1)$ with two parameters $M$ and $P_{\rm cr}$ was initially proposed for Cam clay [*Schofield and Wroth*, 1968]. This yield surface has a pointed vertex at the tip, but in subsequent models the yield function for Cam clay is often prescribed to give elliptic yield caps [*Desai and Siriwardane*, 1984; *Wood*, 1990; *Guéguen et al.*, 2004]. *Carroll* [1991] initially considered a parabolic yield envelope, which he then generalized to a cap of the form $(P - C)^2/A^2 + Q^{1+\kappa}/B^2 = 1$, which gives an ellipse when $\kappa = 1$. Our choice of an elliptical cap is motivated by the extensive data of *Wong et al.* [1997] for the initial yield stresses at the onset of shear-enhanced compaction which are in good agreement with the ellipse

$$\frac{(P/P^* - \gamma)^2}{(1 - \gamma)^2} + \frac{(Q/P^*)^2}{\delta^2} = 1 \tag{3b}$$

in terms of the stresses normalized by the critical pressure $P^*$ for onset of pore collapse. Data for 7 sandstones with porosities ranging from 14% to 35% were observed to fit elliptic caps with $\gamma = c_o/(3P^*) = C_o/P^* \sim 0.5$ and $\delta = b_o/(\sqrt{3}P^*) = B_o/P^*$ ranging from 0.5 to 0.7 [*Wong et al.*, 1997].

### 3.2. Carroll's Critical State Model

[23] The evolution of the yield envelop in *Carroll*'s [1991] model as a function of plastic volumetric strain

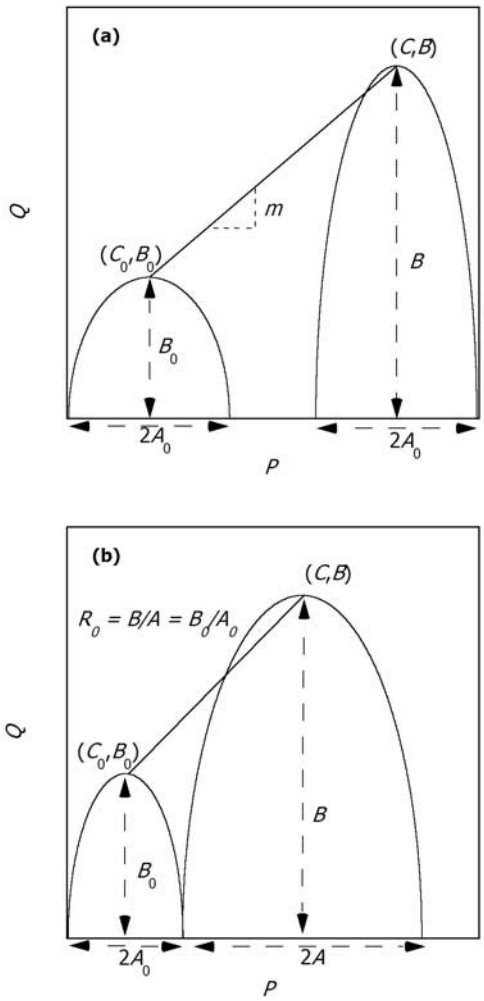


**Figure 3.** (a) Schematic diagram illustrating evolution of the yield envelope in the effective mean stress–differential stress space for *Carroll*'s [1991] critical state model. With increasing plastic volumetric strain, the peak of the yield surface with coordinates ($C$, $B$) traverses the critical state line of slope $m$. The width $2A_o$ of the elliptical yield surfaces remains constant. (b) Schematic diagram illustrating evolution of the yield envelope in the effective mean stress–differential stress space for *DiMaggio and Sandler*'s [1971] cap model. The aspect ratio $B/A$ of the elliptical caps remains constant with increasing plastic volumetric strain.

during work hardening is illustrated by the schematic diagram in Figure 3a. The three parameters for the ellipse are subjected to two constraints. (1) One of the semiaxis remains constant so that $A = A_o$ even if $\varepsilon_v^p$ becomes greater than zero. (2) The other two parameters are related to one another, in that they are required to satisfy

$$B = B_o + m(C - C_o) \tag{4a}$$

As illustrated in Figure 3a, this second condition imposes the rather stringent constraint that the yield cap will always evolve with its tip located at ($C$, $B$) moving along the "critical state line" with slope $m$ (Figure 3a), or equivalently, the coordinates ($c$, $b$) always fall on the line

$$b = b_o + \left(m/3^*\sqrt{3}\right)(c - c_o) \tag{4b}$$

This second condition is the primary attribute that characterizes a critical state model. Nevertheless, it should also be emphasized that *Carroll*'s [1991] model is different in one important aspect from models in critical state soil mechanics which typically assume that the ellipse would pass through the origin and therefore the equality $C = A$ holds at every stage of strain hardening. For a cohesive rock undergoing strain hardening it is unlikely that the yield envelope would pass through the origin.

[24] To compare the constitutive model prediction with laboratory data, it was necessary to map out contours in the stress space corresponding to specific values of plastic volumetric strain. Since in a sandstone plastic deformation of the solid grains is negligible at room temperature under the pressure conditions in our experiments, the plastic porosity change $\Delta\Phi^p$ represents the bulk of the plastic volumetric strain, and to a first approximation we can take $\varepsilon_v^p = \Delta\Phi^p$ (with the convention that $\Delta\Phi^p$ is positive for compaction). From a plot of the total porosity change versus effective mean stress (Figures 1a, 1c, and 2b) the plastic porosity change $\Delta\Phi^p$ at a given point beyond $C^*$ was evaluated by subtracting from the total porosity change $\Delta\Phi$ the elastic porosity change which is assumed to be given by the linear portion during initial loading.

[25] The stress states attained at constant values of $\varepsilon_v^p$ (inferred from $\Delta\Phi^p$) in triaxial compression experiments for the 4 sandstones were compiled and plotted in Figure 4. To compare with the model prediction, we first fitted the initial yield stress data to an elliptic envelope, thus obtaining values of $A_o$, $B_o$, and $C_o$. We then fitted the subsequent yield stresses for selected values of $\Delta\varepsilon_v^p > 0$ to elliptic envelopes, imposing the equality $A = A_o$. These ellipses are shown in Figure 4, and the coordinates ($C$, $B$) so determined for the elliptic envelopes are plotted in Figure 5. We can then test the "critical state" constraint by checking whether the coordinates ($C$, $B$) at the tip of the elliptic caps do indeed lie on a straight line. For those data that fall on a linear trend the critical state parameters $m$ were evaluated by linear regression and compiled in Table 3.

[26] The Bentheim sandstone data can be fitted with ellipses (with constant $A_o$ = 202 MPa) up to plastic volumetric strain of 0.05 (Figure 4a), while the Adamswiller sandstone data can be fitted with ellipses (with $A_o$ = 98 MPa) up to plastic volumetric strain of 0.02 (Figure 4b). We also include for the latter yield stress data for $\Delta\varepsilon_v^p = 0.03$, but it can be seen that since the plastic volumetric strain from 0.02 to 0.03 was accompanied by a hardening rate that was significantly higher for hydrostatic loading than triaxial loading, the Adamswiller sandstone data at the higher plastic strain cannot be reasonably fit with an ellipse with constant $A_o$. For the Berea (Figure 4c) and Darley Dale (Figure 4d) sandstones, the yield stress data can be fitted by ellipses with constant $A_o$ only at relatively small plastic strains of $\Delta\varepsilon_v^p \leq 0.01$ (Figure 4c) and $\Delta\varepsilon_v^p \leq 0.0025$ (Figure 4d), respectively. It should be

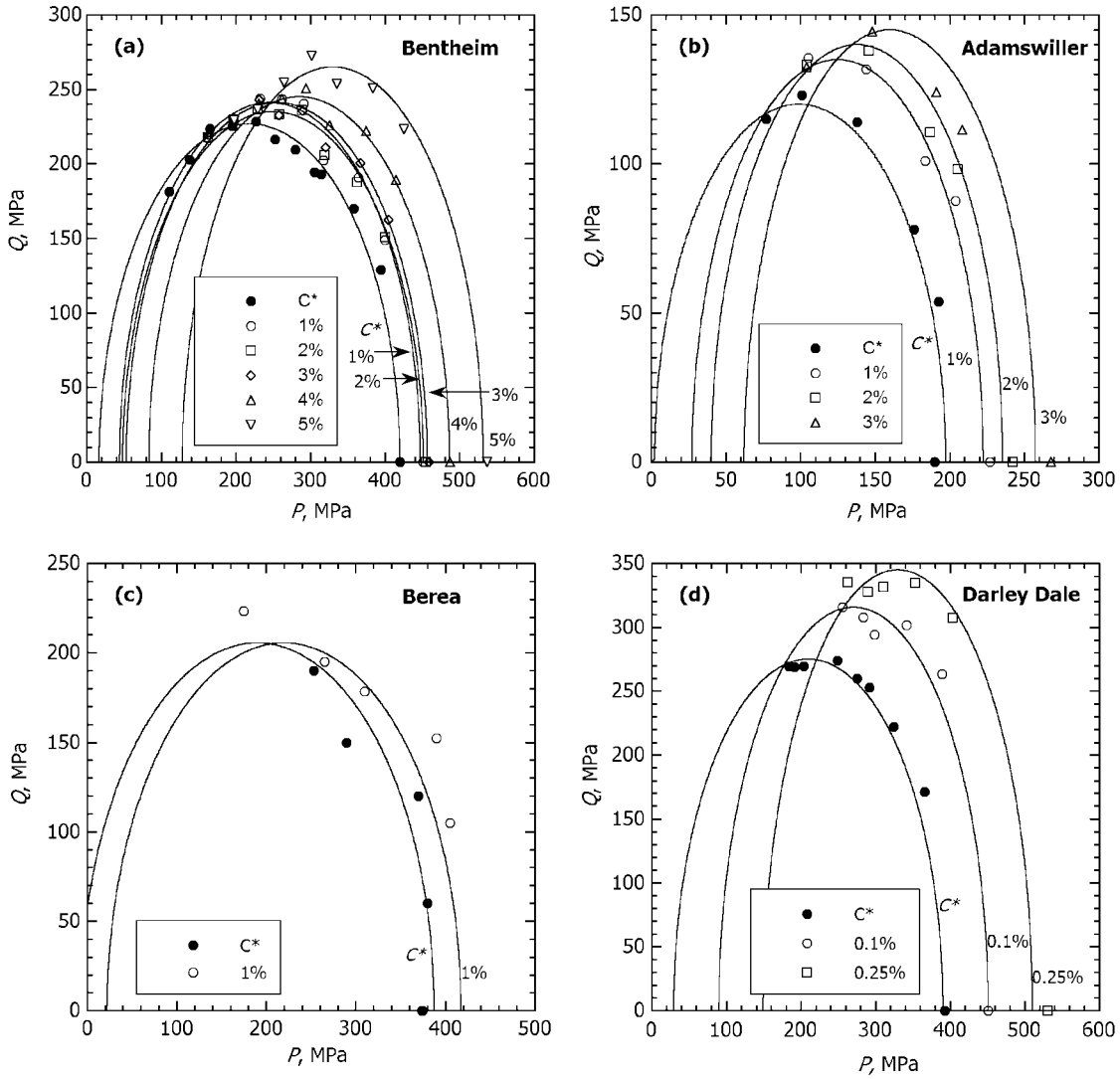


**Figure 4.** Comparison between *Carroll*'s [1991] critical state model and experimental data on the initial yield stress $C^*$ and evolution of the yield stress as a function of plastic volumetric strain for (a) Bentheim, (b) Adamswiller, (c) Berea, and (d) Darley Dale sandstones. Geometric parameters for the elliptical envelopes are compiled in Table 3.

noted that the data for Berea sandstone presented in Figure 4c are the data from *Wong et al.* [1992] which reached larger plastic volumetric strain.

[27] It can be seen in Figure 5 that the Adamswiller, Bentheim, and Darley Dale sandstone data fall on the predicted linear trends with "critical state" slopes of 0.54, 0.32, and 0.58, respectively. There seems to be a trend for the slope $m$ to increase with decreasing porosity. Since the Berea sandstone data could be fitted with elliptic envelopes over a very limited range, we did not attempt to fit them with a critical state line.

### 3.3. DiMaggio-Sandler Cap Model

[28] The evolution of the yield cap in *DiMaggio and Sandler*'s [1971] model as a function of plastic volumetric strain is illustrated by the schematic diagram in Figure 3b. In contrast to *Carroll*'s [1991] model, the parameters of the ellipse have more degrees of freedom since only one constraint is imposed here: the aspect ratio of the cap remains constant, so that

$$B/A = B_o/A_o = R_o \tag{5}$$

as the rock undergoes work hardening. To compare our data with this cap model, we fitted the initial and subsequent yield stresses for selected values of $\varepsilon_v^p > 0$ to elliptic caps without imposing any constraints (Figure 6). If indeed the yield behavior was as predicted by DiMaggio-Sandler cap model, then the value of $R$ for each sandstone should remain the same as it strain hardens. The aspect ratios $R = B/A$ so determined for the yield caps are plotted in Figure 7. The cap model parameters for these four sandstones are also compiled in Table 3.

[29] Yield stress data for the Bentheim sandstone can be fitted reasonably well with elliptic caps up to plastic volumetric strain of 0.06 (Figure 6a). For Adamswiller sandstone we show in Figure 6b elliptic caps up to $\Delta\varepsilon_v^p =$

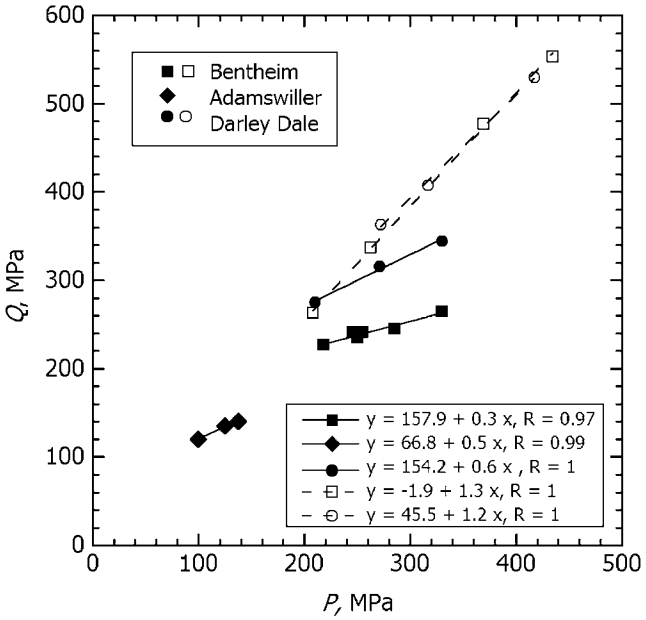


**Figure 5.** Coordinates for the peaks of the yield envelopes (in Figures 4a, 4b, and 4d) (shown by solid symbols) and the critical stresses $C^{*\prime}$ for the transition from compactancy to dilatancy (shown by open symbols). The critical state lines can be inferred from these experimental data using two different approaches. (1) Linear fits to the solid symbols represent the critical state lines according to *Carroll*'s [1991] model. (2) If the normality condition applies, then $C^{*\prime}$ should also represent the critical state. That the lines inferred using different approaches for a sandstone do not coincide is attributed to nonassociative behavior. The lines were obtained by linear regression.

0.05, but it should be noted that the fits are somewhat marginal for $\Delta\varepsilon_v^p$ = 0.04 and 0.05. For Berea sandstone (Figure 6c) the elliptic caps were acceptable given the significant scatter in the data [from *Wong et al.*, 1992], while the fit to the Darley Dale sandstone data (Figure 6d) is very good.

[30] It can be seen from Figures 7a and 7c that in agreement with the DiMaggio and Sandler model the aspect ratios of the caps for both Bentheim and Berea sandstone were approximately constant, with arithmetic means of 1.16 and 1.08, respectively (Table 3). In contrast the aspect ratios of Adamswiller (Figure 7c) and Darley Dale (Figure 7d) sandstones decreased rapidly with increasing plastic strain, implying that the DiMaggio and Sandler cap model is not applicable.

### 3.4. Normality Condition and Associated Flow Rule

[31] Other than the yield stresses a constitutive model should also specify how plastic flow develops after the rock has yielded. In plasticity theory the conventional approach is to assume that the inelastic deformation follows *Drucker*'s [1951] postulate of material stability, and accordingly a flow rule can be associated with the yield function by

$$\Delta\varepsilon_{ij}^p = \frac{\partial f}{\partial \sigma_{ij}}\Delta\lambda \tag{6}$$

where $\Delta\varepsilon_{ij}^p$ denotes the plastic increment of the strain tensor and $\Delta\lambda$ is a positive scalar. Since equation (6) implies that the plastic strain tensor will be oriented perpendicular to the yield surface, it is also called the "normality condition" [*Desai and Siriwardane*, 1984; *Davis and Selvadurai*, 2002]. While such an associated flow rule specifies all six components of the strain tensor, we have independent measurements of only two strain components for the axisymmetric configuration of a conventional triaxial test. Since our primary data are in terms of the axial strain and porosity change, we will focus on the constitutive modeling of these two strains for comparison with laboratory results.

**Table 3.** Critical State and Cap Model Parameters for the Four Sandstones Investigated in This Study

| Plastic Volumetric Strain, % | *B*, MPa | *C*, MPa | *B*/*A* |
|---|---|---|---|
| *Darley Dale: Critical State ($A_0$ = 180 MPa; m = 0.58)* | | | |
| 0 | 275 | 210 | 1.53 |
| 0.1 | 316 | 271 | 1.76 |
| 0.25 | 345 | 330 | 1.92 |
| *Darley Dale: Cap Model* | | | |
| 0 | 277 | 228 | 1.82 |
| 0.1 | 316 | 271 | 1.75 |
| 0.25 | 340 | 308 | 1.52 |
| 0.5 | 371 | 377 | 1.3 |
| *Berea: Cap model* | | | |
| 0 | 198 | 190 | 1.04 |
| 1 | 213 | 205 | 1.04 |
| 3.5 | 290 | 250 | 1.16 |
| *Adamswiller: Critical State ($A_0$ = 98 MPa; m = 0.54)* | | | |
| 0 | 120 | 100 | 1.22 |
| 1 | 135 | 125 | 1.38 |
| 2 | 140 | 138 | 1.43 |
| 3 | 145 | 160 | 1.48 |
| *Adamswiller: Cap Model* | | | |
| 0 | 125 | 109 | 1.51 |
| 1 | 136 | 125 | 1.33 |
| 2 | 137 | 135 | 1.3 |
| 3 | 140 | 143 | 1.15 |
| 4 | 158 | 176 | 1.14 |
| 5 | 177 | 212 | 1.02 |
| *Bentheim: Critical State ($A_0$ = 202 MPa; m = 0.32)* | | | |
| 0 | 227 | 218 | 1.12 |
| 1 | 241 | 246 | 1.19 |
| 2 | 235 | 250 | 1.16 |
| 3 | 241 | 255 | 1.19 |
| 4 | 245 | 285 | 1.21 |
| 5 | 265 | 330 | 1.31 |
| *Bentheim: Cap Model* | | | |
| 0 | 227 | 218 | 1.13 |
| 1 | 241 | 246 | 1.15 |
| 2 | 237 | 241 | 1.11 |
| 3 | 239 | 243 | 1.11 |
| 4 | 248 | 273 | 1.16 |
| 5 | 268 | 316 | 1.22 |
| 6 | 295 | 348 | 1.22 |

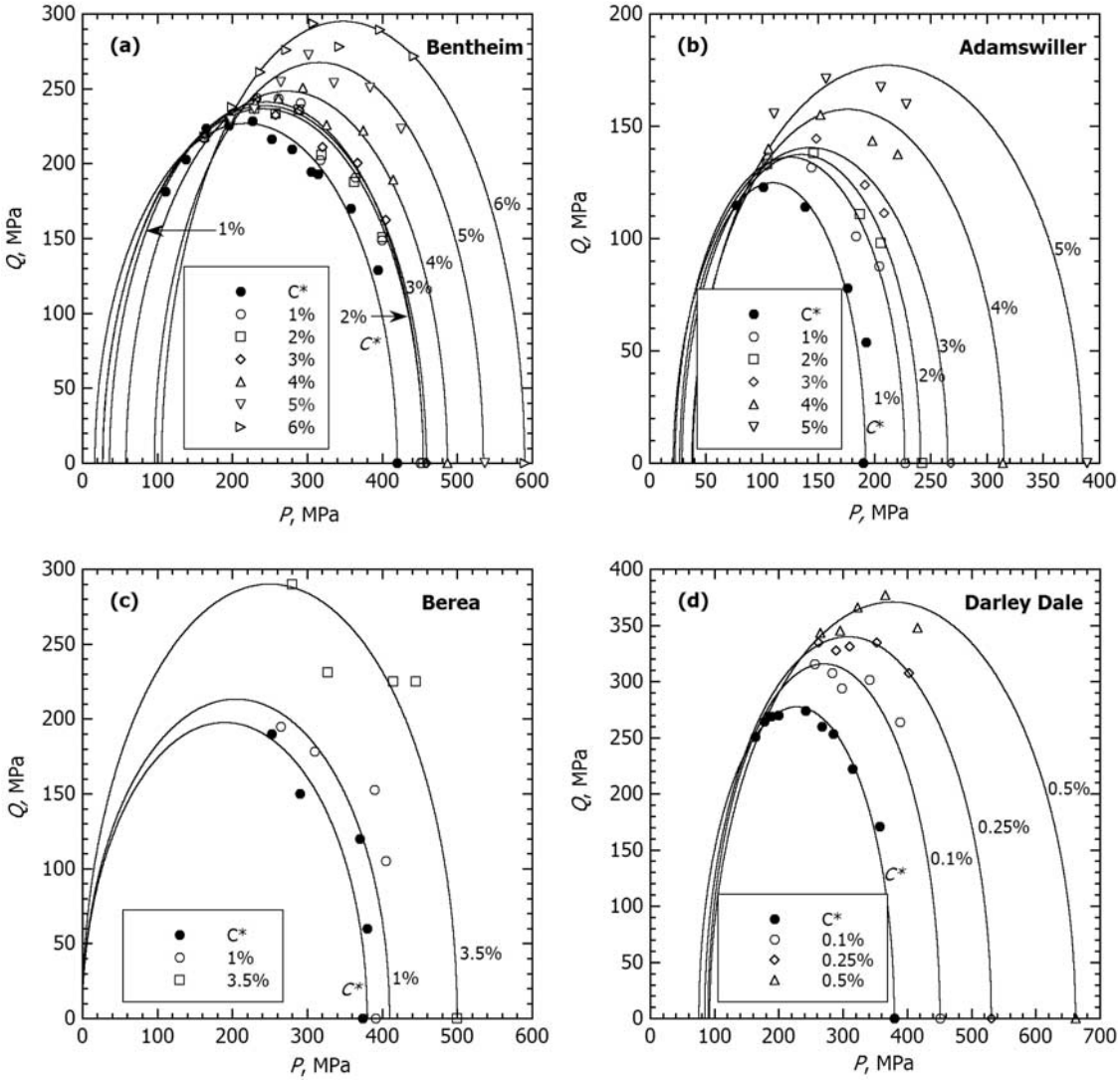


**Figure 6.** Comparison between *DiMaggio and Sandler*'s [1971] cap model and experimental data on the initial yield stress $C^*$ and evolution of the yield stress as a function of plastic volumetric strain for (a) Bentheim, (b) Adamswiller, (c) Berea, and (d) Darley Dale sandstones. Geometric parameters for the elliptical envelopes are compiled in Table 3.

[32] The ratio between the volumetric and axial components of the plastic strain can be derived by substituting the yield function (2) into the normality condition (6):

$$\frac{\Delta\varepsilon_{ii}^p}{\Delta\varepsilon_{11}^p} = \frac{18b^2(I_1 - c)}{a^2(2\sigma_{11} - \sigma_{22} - \sigma_{33}) + 6b^2(I_1 - c)} \tag{7a}$$

For a conventional triaxial test if we denote the volumetric component by $\Delta\varepsilon_v^p = \Delta\varepsilon_{ii}^p$ and axial component by $\Delta\varepsilon^p = \Delta\varepsilon_{11}^p$, then the above ratio reduces to

$$\frac{\Delta\varepsilon_v^p}{\Delta\varepsilon^p} = \frac{3}{(3A^2/B^2)(Q/(P - C)) + 1} \tag{7b}$$

Two important consequences of the normality condition can be noted from equation (7b). First, it predicts that the volume contracts (or expands) for effective mean stress $P$ greater (or less) than $C$. In other words a transition in deformation mode from compactancy to dilatancy occurs at the tip of the yield envelope located at ($C$, $B$). At this transition point the porous material is considered to be at the "critical state". However, it should be noted that some of our data points for compactive yield stress (Figure 6) actually fall on the side of the ellipse $P < C$, thus contradicting the normality prediction that at relatively low mean stresses the sample would yield by dilatancy and not compactancy. Second, under hydrostatic loading ($Q = 0$) the increment of plastic volumetric strain is three times the increment of axial strain, which of course applies only if the behavior is isotropic. *Wong and Baud* [1999] presented strain data for hydrostatic compaction of nominally dry samples of Berea and Darley Dale sandstones that agree with this prediction.

[33] To test the normality condition on experimental data, we first note as before that the plastic component of volumetric strain is dominated by porosity change, and hence the ratio $\Delta\varepsilon_v^p/\Delta\varepsilon^p \approx \Delta\Phi^p/\Delta\varepsilon^p$. Accordingly the

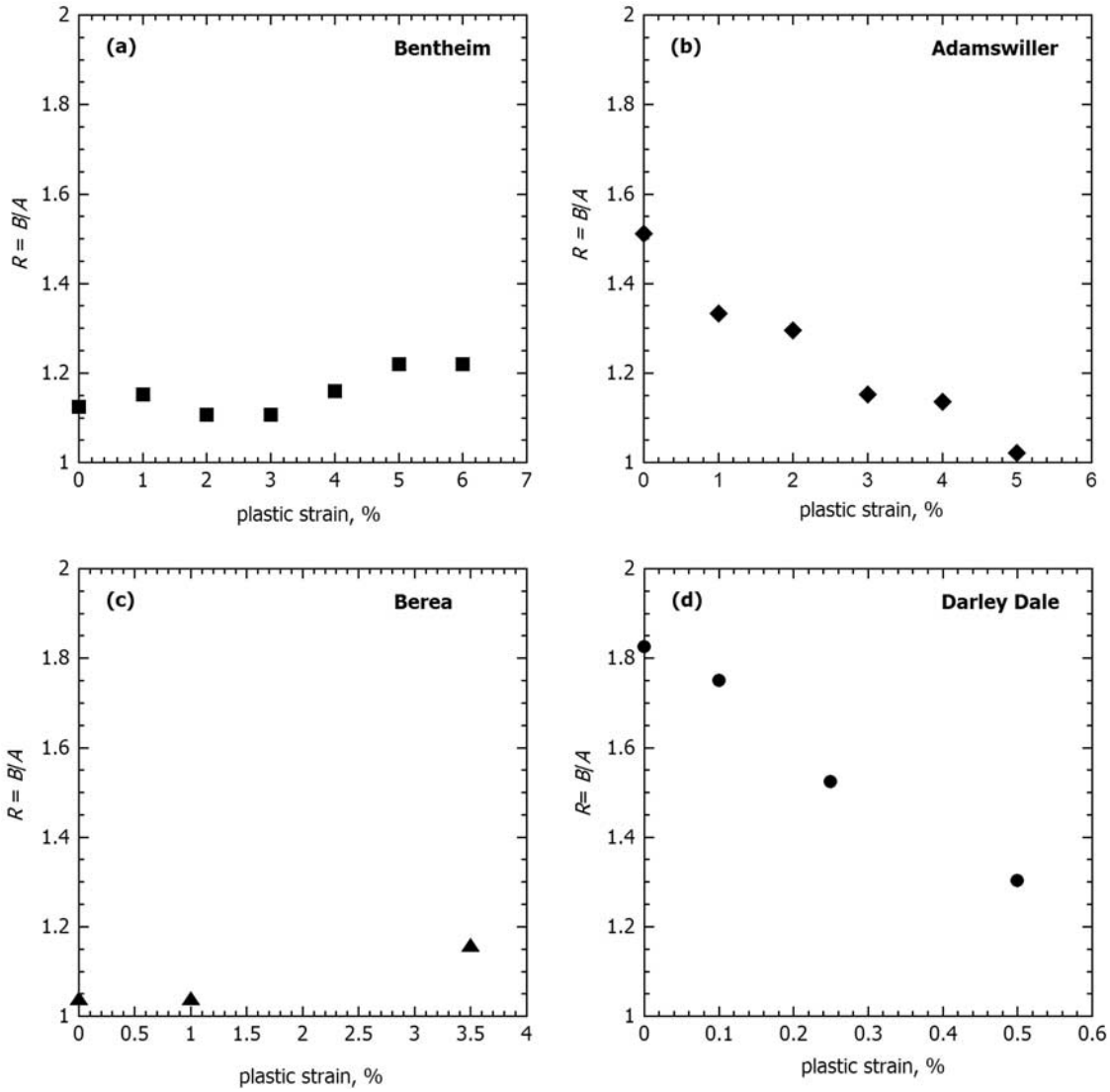


**Figure 7.** Aspect ratio of the elliptical yield caps (shown in Figure 6) as a function of plastic volumetric strain for (a) Bentheim, (b) Adamswiller, (c) Berea, and (d) Darley Dale sandstones. According to the *DiMaggio and Sandler*'s [1971] cap model the aspect ratio should remain constant.

model prediction (7b) for $\Delta\varepsilon_v^p/\Delta\varepsilon^p$ can be compared with the "inelastic compaction factor" $\Delta\Phi^p/\Delta\varepsilon^p$, which we can infer from our laboratory data following the methodology described in detail by *Wong et al.* [1997]. From the slope of the curve for the porosity change as a function of axial strain the ratio between incremental change of the porosity $\Phi$ and axial strain $\varepsilon$ can be evaluated. After appropriately subtracting from the total strains the elastic parts, the ratio $\Delta\Phi^p/\Delta\varepsilon^p$ was then evaluated.

[34] In Figure 8 we plot the inelastic compaction factor $\Delta\Phi^p/\Delta\varepsilon^p$ as a function of effective pressures for selected values of plastic volumetric strain. For comparison we also show theoretical predictions according to (7b) for the flow rules associated with the elliptic yield caps shown in Figure 6. Because of significant scatter in the Berea sandstone data, we only evaluated the compaction factors for its initial yield data. With the exception of one data point (corresponding to the initial yield stress of Darley Dale sandstone at an effective pressure of 300 MPa) all our measurements fall in the range of $0 < \Delta\Phi^p/\Delta\varepsilon^p < 1$, with the implication that $0 < d\varepsilon_v^p < d\varepsilon_1^p$. Since $d\varepsilon_v^p = d\varepsilon_1^p + 2d\varepsilon_3^p$ in a conventional triaxial experiment, our data require that inelastic yield in these sandstones to be accompanied by an overall reduction in volume that involves the interplay of axial shortening ($d\varepsilon_1^p > 0$) and lateral expansion ($d\varepsilon_2^p = d\varepsilon_3^p < 0$). More specifically if we follow *Deshpande and Fleck* [2000] to define the "plastic Poisson's ratio" by $\nu^p = -d\varepsilon_3^p/d\varepsilon_1^p$, then basically all our data fall in the range $0.5 > \nu^p > 0$.

[35] Among the four Darley Dale (Figure 8d) sandstone shows the best agreement with the prediction of the associated flow rule. In contrast the shear-enhanced compaction observed in both Bentheim (Figure 8a) and Berea sandstones (Figure 8c) was appreciably more than what is predicted for associative behavior, especially at relatively low mean stresses. In these two sandstones the lateral expansion of a yielded sample (and therefore the plastic Poisson's ratio $0.5 > \nu^p > 0$) was generally less than that prescribed by the normality condition. The behavior of

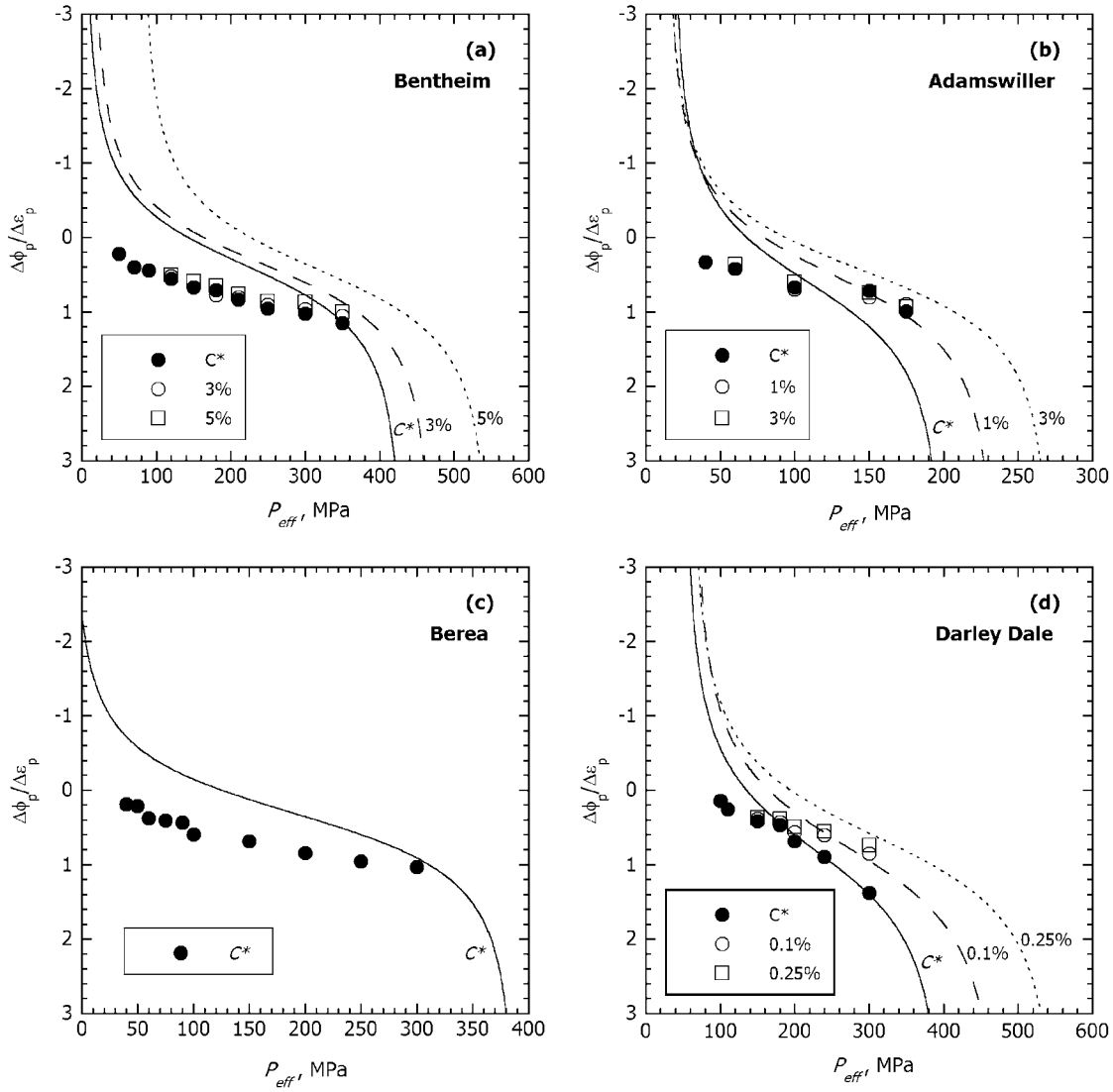


**Figure 8.** Comparison of experimental data with prediction of the normality condition in (a) Bentheim, (b) Adamswiller, (c) Berea, and (d) Darley Dale sandstones. The inelastic compaction factor at the onset of shear-enhanced compaction $C^*$ and increasing plastic volumetric strain as a function of the effective pressure at which a triaxial compression experiment was conducted. Solid lines represent the theoretical predictions for associative behavior according to equation (7b).

Adamswiller sandstone (Figure 8b) was most complicated, with inelastic compaction that was lower than predicted at relatively high mean stresses and higher at low mean stresses. This comparison indicates that it is necessary to introduce a constitutive model that does not hinge on the normality assumption if one were to realistically model the inelastic deformation of these sandstones over a broad range of effective pressure.

### 3.5. Nonassociated Flow Rule and Localization Analysis

[36] A nonassociative model necessarily involves a plastic potential function and additional constitutive parameters. As an example we will focus on a nonassociative model originally formulated by *Rudnicki and Rice* [1975] for analyzing the onset of shear localization in a dilatant frictional material. In this isotropic hardening model three constitutive parameters (in addition to two elastic moduli) were used for characterizing the inelastic and failure behavior: an internal friction parameter $\mu$, a dilatancy factor $\beta$, and a hardening modulus $h$. The flow law is associative only if $\beta = \mu$.

[37] As elaborated by *Wong et al.* [1997], the constitutive parameters can be extracted from triaxial compression experiment data in the following manner. If we assume that $\Delta\varepsilon_v^p \approx \Delta\Phi^p$, then the dilatancy factor $\beta$ in *Rudnicki and Rice*'s [1975] model is related to the inelastic compaction factor by

$$\beta = -\sqrt{3}\frac{\Delta\Phi^p/\Delta\varepsilon^p}{(3 - \Delta\Phi^p/\Delta\varepsilon^p)}. \tag{8a}$$

The parameter $\beta$ can therefore be derived from the $\Delta\Phi^p/\Delta\varepsilon^p$ values evaluated from laboratory data as discussed

above. The difference in sign convention between the dilatancy and compaction factors should be noted: if $\Delta\Phi^p/\Delta\varepsilon^p < 0$, then $\beta > 0$. As for the "friction" parameter $\mu$ it can be evaluated as $\sqrt{3}/3$ times the local slope of the yield envelope in the $P$-$Q$ space, or explicitly in terms of the parameters for an elliptic cap as

$$\mu = -\frac{B^2(P-C)}{\sqrt{3}A^2Q}. \tag{8b}$$

We used values of $P$ and $Q$ directly from our laboratory data, and the elliptic cap parameters $A$, $B$ and $C$ were for the ellipses that fit the yield stresses shown in Figure 6. The hardening modulus $h$ is defined e.g., by *Paterson and Wong* [2005] in their equation A2.20c. Its value is positive for strain hardening and negative for strain softening [*Wong et al.*, 1997]. Using equations (8a) and (8b) we evaluated $\mu$ and $\beta$ in the Rudnicki and Rice model from our initial yield data at the onset of shear-enhanced compaction, which are plotted in Figures 9a–9d with the failure mode indicated.

[38] Negative values of $\beta$ are associated with samples that yield by shear-enhanced compaction and fail by the development of one of three modes typical of this regime: high-angle shear bands, compaction bands, or homogeneous cataclastic flow [*Wong et al.*, 2001; *Baud et al.*, 2004]. A "compaction band" is defined to be a localized structure subperpendicular to $\sigma_1$, whereas a "high-angle shear band" is a localized structure that subtends a relatively high angle (say 45–80°) to $\sigma_1$. A localized structure that extends laterally over only a few (say $\leq 3$) grains is referred to as a "discrete band", whereas a structure that extends laterally over many grains is called a "diffuse band". Darley Dale is the only sandstone with approximately equal values of $\beta$ and $\mu$ (Figure 9d), in agreement with the earlier observation that its behavior satisfies the normality condition. On the other hand the nonassociative behavior in the other three sandstones results in $\mu \neq \beta$ (Figures 9a–9c). In the compactive yield regime, with increasing effective mean stress the value of $\mu$ typically decreases from a slightly positive value through zero (at the tip of the cap) to negative.

[39] For reference we also include in Figures 9a–9d data for samples that failed by dilatant faulting with development of shear bands. Following the procedure outlined by *Wong et al.* [1997], we evaluated the parameters $\beta$ and $\mu$ at the peak stresses using the mechanical data for Darley Dale and Berea sandstones presented by *Baud et al.* [2000a, 2000b], for Adamswiller sandstone by *Wong et al.* [1997], and for saturated Bentheim sandstone (at effective pressures of 10, 20 and 30 MPa) acquired in this study. In the dilatant faulting regime the value of $\beta$ is positive. It typically decreases with increasing effective mean stress, while the value of $\mu$ remains relatively constant corresponding to a Coulomb failure envelope with an almost constant coefficient of internal friction.

[40] The data summarized in Figures 9a–9d show that as a porous sandstone undergoes the brittle-ductile transition, the failure mode evolves from shear band to compaction band to homogeneous cataclastic flow as the constitutive parameters $\beta$ and $\mu$ decrease with increasing effective pressure. Bifurcation analyses [*Rudnicki and Rice*, 1975; *Olsson*, 1999; *Issen and Rudnicki*, 2000] specify the critical conditions for the onset of strain localization, thus providing a theoretical framework for understanding how this transition in failure mode arises from constitutive behavior. If we focus on *Rudnicki and Rice*'s [1975] nonassociative model, then the critical conditions under which dilation, shear or compaction bands would develop are available from *Issen and Rudnicki*'s [2000] analysis. Figure 9e summarizes their results for axisymmetric compression by mapping out the failure mode as a function of the constitutive parameters $\beta$ and $\mu$. If Poisson's ratio is denoted by $\nu$ (for elastic materials), then shear bands are predicted to develop for

$$\sqrt{3} \leq \mu + \beta \leq \sqrt{3}(2-\nu)/(1+\nu) \tag{9a}$$

In contrast, dilation bands (subparallel to $\sigma_1$) would develop if

$$\mu + \beta > \sqrt{3}(2-\nu)/(1+\nu) \tag{9b}$$

and compaction bands would develop if

$$\mu + \beta < -\sqrt{3} \tag{9c}$$

Hence the localization analysis predicts that the brittle-ductile transition is associated with decreasing $\beta$ and $\mu$, in qualitative agreement with the laboratory observations.

[41] The bifurcation analysis also prescribes the critical value of hardening modulus at the onset of strain localization; whether the modulus is predicted to be positive or negative is indicated in Figure 9e. For comparison we also plotted the parameters $\beta$ and $\mu$ for all our samples that developed compaction bands or high-angle shear bands while undergoing shear-enhanced compaction with strain hardening. It can be seen that most of these samples had $\beta$ and $\mu$ values for which the bifurcation analysis predicts shear band formation while the sample undergoes strain softening. In Bentheim sandstone localized compactant failure developed while a sample showed episodic stress drops and strain softening (Figure 1), but the failure mode was dominantly formation of discrete compaction bands and not shear bands as predicted. In the other three sandstones the failure mode was dominantly the formation of high-angle shear bands, but typically they developed while the sample showed strain hardening (Figure 2) and not softening as predicted. A similar conclusion on the basis of data for dry Bentheim sandstone and preliminary data for wet Berea and Darley Dale sandstones was also made by *Wong et al.* [2001], who attributed this discrepancy between experimental observations and localization analysis to the inadequacy of the constitutive model to comprehensively capture the partitioning of several damage mechanisms, including the growth and coalescence of stress-induced microcracks, collapse of pores and crushing of grains.

## 4. Summary and Discussion

[42] Under high confinement a porous rock deforms inelastically by shear-enhanced compaction and strain hardening and ultimately fails with a mode that is conventionally described as homogeneous cataclastic flow, but recent

studies have also documented the occurrence of other possible failure modes such as compaction band formation. To capture the inelastic and failure behaviors, a constitutive model based on plasticity theory should first be validated by laboratory data on the initial yield stresses and their evolution with strain hardening. When used in conjunction with bifurcation analysis, the constitutive model should be able to predict the failure mode and critical conditions for the onset of instability.

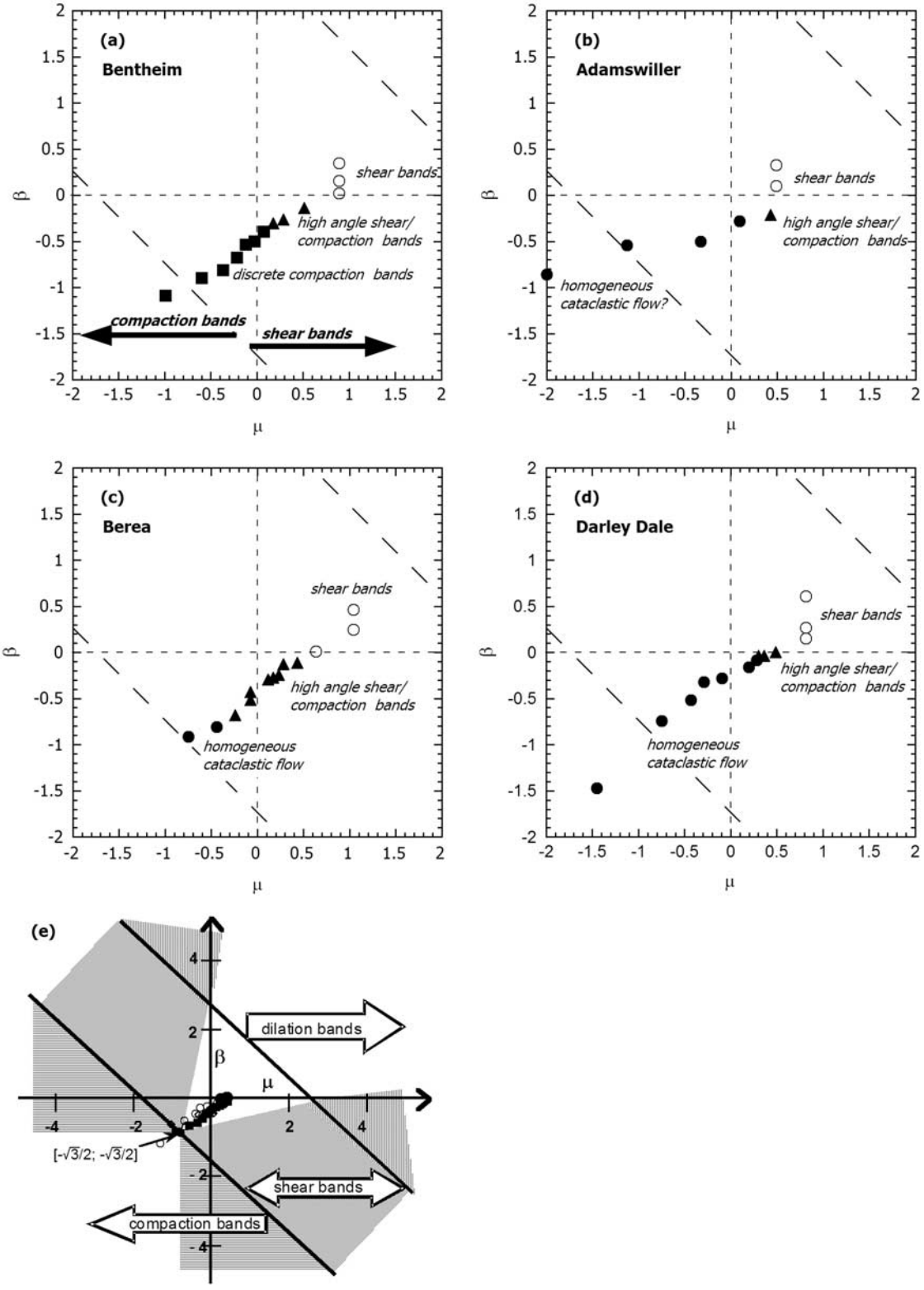


**Figure 9**

[43] In the past decade extensive studies have been made on the initial yield stresses at the onset of shear-enhanced compaction in porous sandstones [e.g., *Wong et al.*, 1997; *Baud et al.*, 2000a, 2000b; *Cuss et al.*, 2003] and sediments [*Chuhan et al.*, 2002; *Chester et al.*, 2004]. The laboratory data show that the critical stress $C^*$ for the onset of shear-enhanced compaction decreases with increasing porosity and grain size, and in terms of the effective mean stress and differential stress the initial yield envelope maps out an elliptic cap in the stress space. Such an elliptic cap has been adopted to model the stress profile, tectonic evolution and fluid flow in sedimentary formations [*Fisher et al.*, 1999; *Casey and Butler*, 2004; *Karner et al.*, 2005; *Bjorlykke et al.*, 2005], borehole instability [*Coelho et al.*, 2005], and initiation of compaction localization due to geometric heterogeneity [*Tembe et al.*, 2006]. In this study we move beyond the initial yield stage to consider the subsequent evolution of the yield stresses after the onset of shear-enhanced compaction. Our data for four saturated sandstones show that the subsequent yield stresses can also be characterized by elliptic caps if we assume that the strain hardening behavior depends solely on the plastic volumetric strain. While our analysis is based on mechanical data from triaxial compression tests under drained condition, it is of interest to note that recent data of *Tembe et al.* [2005] from undrained experiments on Adamswiller and Diemelstadt sandstones also map out initial and subsequent yield caps that are elliptic in shape.

[44] We compare our data with the predictions of two plasticity models on the evolution of yield surfaces with strain hardening. *Carroll*'s [1991] critical state model prescribes one of the semiaxis of the elliptic cap to be constant and the tip of the cap to move along the critical state line. The yield caps of Adamswiller, Bentheim and Darley Dale sandstones agree with this critical state model up to plastic volumetric strains of 0.02, 0.05 and 0.0025, respectively. *DiMaggio and Sandler*'s [1971] cap model prescribes the aspect ratio of the yield caps to be fixed, and the observed yield caps of Bentheim and Berea sandstones agree with this cap model up to plastic volumetric strains of 0.06 and 0.035, respectively. It should be noted that among the four only Bentheim sandstone shows reasonable agreement with both models up to relatively large strain. These two constitutive models are widely used in geotechnical and geological applications since they involve a relatively small number of parameters. The cap model is built into finite element codes such as ABAQUS [*ABAQUS, Inc.*, 2004] or FLAC3D [*Sheldon et al.*, 2006] for the numerical simulation of inelastic compaction in porous rock [*Vajdova et al.*, 2003; *Grueschow*, 2005], ceramic powder [*Zeuch et al.*, 2001] and pharmaceutical powder [*Wu et al.*, 2005]. Our comparison here underscores the necessity to first characterize experimentally the evolution of compactive yield behavior before selecting the appropriate constitutive model.

[45] The normality condition is implicitly assumed in these formulations of the critical state and cap models. In our experiments Darley Dale sandstone showed the best agreement with the prediction of an associated flow rule. The shear-enhanced compaction observed in both Bentheim and Berea sandstones was appreciably more than what is predicted for an associative flow rule, especially at relatively low mean stresses. In Adamswiller sandstone the behavior was rather complicated, with inelastic compaction that was lower than predicted by normality at relatively high mean stresses and higher at low mean stresses. The implication is that it is necessary to introduce a nonassociative model if one were to realistically capture the inelastic behavior of these sandstones over a broad range of effective pressures. In particular there are two key characteristics of critical state soil mechanics that are not expected to apply to these porous sandstones. First, the tip of the cap separates the yield behavior into two distinct regimes (with compactancy and dilatancy at high and low mean stress stresses, respectively) only if the yield behavior is associative. In porous sandstones compactancy was observed down to relatively low mean stresses at the "other side" of the cap. Second, it is commonly assumed that as a soil undergoes inelastic compaction its porosity would be reduced to ultimately attain the "critical state" corresponding to a transition between compactancy and dilatancy, but if the behavior is nonassociative then this stress state does not necessarily fall on the critical state line (4a) defined by the tips of the elliptic caps. The former description of "critical state" corresponds to the stress states $C^{*\prime}$ (Figures 1 and 2) which we also plotted in Figure 5. It can be seen that while our $C^{*\prime}$ data for Bentheim and Darley Dale sandstones do fall on linear trends, the slopes are significantly steeper than the slope $m$ for the tips of the elliptic caps (equation (4a)). The linear slopes of the $C^{*\prime}$ data are more comparable to the slopes of the Coulomb failure envelopes for the samples that failed by dilatant faulting.

[46] A bifurcation analysis can predict the critical conditions for the onset of strain localization, thus providing a theoretical framework for understanding how the transition in failure mode arises from constitutive behavior. With reference to *Rice and Rudnicki*'s [1975] constitutive model,

**Figure 9.** Constitutive parameters for the nonassociative model of *Rudnicki and Rice* [1975] for (a) Bentheim, (b) Adamswiller, (c) Berea, and (d) Darley Dale sandstones. The solid circles, squares, and triangles correspond to the dilatancy factor $\beta$ as a function of internal friction coefficient $\mu$ at the onset of shear-enhanced compaction for samples that failed by the development of homogeneous cataclastic flow, discrete compaction bands, and high-angle shear/diffuse compaction bands, respectively. The open circles correspond to the constitutive parameters at the peak stress for samples that failed by dilatant faulting. The three failure modes (compaction band, shear band, and dilation band) predicted from bifurcation analysis of *Issen and Rudnicki* [2000] are separated by the diagonal lines $\mu + \beta = -\sqrt{3}$ and $\mu + \beta = \sqrt{3}(2 - \nu)/(1 + \nu)$, where $\nu$ is Poisson's ratio (of elastic materials). (e) Comparison of our data for the onset of shear-enhanced compaction for samples that failed by development of compaction localization (solid symbols) and homogeneous cataclastic flow (open symbols) with failure mode prediction from bifurcation analysis of *Issen and Rudnicki* [2000]. The three failure modes (compaction band, shear band, and dilation band) predicted from bifurcation analysis of *Issen and Rudnicki* [2000] are separated by the diagonal lines $\mu + \beta = -\sqrt{3}$ and $\mu + \beta = \sqrt{3}(2 - \nu)/(1 + \nu)$. For each mode, localization develops during strain hardening ($h > 0$) in the shaded area and during strain softening ($h < 0$) in the unmarked area.

our data show that as a porous sandstone undergoes the brittle-ductile transition the failure mode evolves from shear band to compaction band to homogeneous cataclastic flow as the constitutive parameters $\beta$ and $\mu$ decrease with increasing effective pressure. This agrees qualitatively with the prediction of localization analysis that the transition of failure mode from dilation band to shear band to compaction band is associated with decreasing $\beta$ and $\mu$. However, there is significant discrepancy between the quantitative predictions on the critical parameters at the onset of strain localization and experimental data, which is possibly due to the limitation of the Rudnicki-Rice model to comprehensively capture the partitioning of several operative damage mechanisms, including stress-induced microcracking, pore collapse and grain crushing. It should also be noted that strictly speaking such a continuum formulation should be applied only to a material that has not developed structural heterogeneity in the form of strain localization, unless the constitutive behavior of the localized structure is specified separately. In a rock such as Bentheim sandstone, which develops discrete compaction bands soon after the onset of shear-enhanced compaction [*Baud et al.*, 2004], there may be a limit on the plastic strain beyond which a homogeneous continuum model is no longer appropriate.

[47] A more elaborate constitutive model will necessarily involve many additional parameters. Indeed the mechanical data summarized here have motivated the development of several such models that attempt to account for the possible influence of two yield surfaces [*Issen*, 2002], anisotropy [*Rudnicki*, 2002] and intermediate principal stress (K. A. Issen and V. Challa, Influence of intermediate principal stress on the strain localization mode in porous rocks, submitted to *Journal of Geophysical Research*, 2005). These more involved models can predict the development of compaction bands over a wider range of conditions while the porous rock strain hardens. It was also postulated by *Grueschow and Rudnicki* [2005] that the yield cap for porous sandstone should evolve as a function of not only the plastic volumetric strain but also the shear strain. In this study we have restricted the comparison to plasticity models, but it should be noted that alternative models involving plastic pore collapse, two-phase medium and damage mechanics [e.g., *Curran and Carroll*, 1979; *Ricard and Bercovici*, 2003; *Hamiel et al.*, 2004] have been developed to derive the yield surface of porous rocks. Porous sandstone is the focus of the present study, but *Vajdova et al.* [2004b] have demonstrated that the phenomenology of compactive yield and failure in porous carbonate rocks is very similar. Indeed it is of interest to extend the present investigation to other rock types and constitutive models.

[48] **Acknowledgments.** We have benefited from discussions with John Rudnicki, Florian Lehner, Mervyn Paterson, Eric Grueschow, Joanne Fredrich, Kathleen Issen, Laurent Louis, Sheryl Tembe, and Wenlu Zhu. We are grateful to Ernie Rutter and one anonymous reviewer for thoughtful reviews. This research was partially supported by the Office of Basic Energy Sciences, Department of Energy under grant DE-FG02-99ER14996.

## References

ABAQUS, Inc. (2004), ABAQUS theory manual, version 6.3, Providence, R. I.

Baud, P., W. Zhu, and T. Wong (2000a), Failure mode and weakening effect of water on sandstone, *J. Geophys. Res.*, *105*, 16,371–16,389.

Baud, P., A. Schubnel, and T. Wong (2000b), Dilatancy, compaction and failure mode in Solnhofen limestone, *J. Geophys. Res.*, *105*, 19,289–19,303.

Baud, P., E. Klein, and T. Wong (2004), Compaction localization in porous sandstones: Spatial evolution of damage and acoustic emission activity, *J. Struct. Geol.*, *126*, 603–624.

Baud, P., L. Louis, C. David, G. Rawlings, and T. Wong (2005), Effects of bedding and foliation on mechanical anisotropy, damage evolution and failure mode, in High-Strain Zones: Structure and Physical Properties, edited by D. Bruhn and L. Burlini, *Geol. Soc. Spec. Publ.*, *245*, 223–249.

Bjorlykke, K., K. Hoeg, J. I. Faleide, and J. Jahren (2005), When do faults in sedimentary basins leak? Stress and deformation in sedimentary basins; examples from the North Sea and Haltenbanken, offshore Norway, *AAPG Bull.*, *89*, 1019–1031.

Byerlee, J. (1990), Friction, overpressure and fault normal compression, *Geophys. Res. Lett.*, *17*, 2109–2112.

Byrne, T., A. Maltman, E. Stephenson, W. Soh, and R. Knipe (1993), Deformation structures and fluid flow in the toe region of the Nankai accretionary prism, *Proc. Ocean Drill. Program Sci. Results*, *131*, 83–192.

Carroll, M. M. (1991), A critical state plasticity theory for porous reservoir rock, in *Recent Advances in Mechanics of Structured Continua*, vol. 117, edited by M. Massoudi and K. R. Rajagopal, Am. Soc. of Mech. Eng., New York.

Casey, M., and R. W. H. Butler (2004), Modelling approaches to understanding fold development: Implications for hydrocarbon reservoirs, *Mar. Pet. Geol.*, *21*, 933–946.

Chen, W. F. (1984), Soil mechanics, plasticity and landslides, in *Mechanics of Inelastic Materials*, edited by G. J. Dvorak and R. T. Shield, pp. 31–58, Elsevier, New York.

Chester, J. S., S. C. Lenz, F. M. Chester, and R. A. Lang (2004), Mechanisms of compaction of quartz sand at diagenetic conditions, *Earth Planet. Sci. Lett.*, *220*, 435–451.

Chuhan, F. A., A. Kjeldstad, K. Bjørlykke, and K. Høeg (2002), Porosity loss in sand by grain crushing—Experimental evidence and relevance to reservoir quality, *Mar. Petrol. Geol.*, *19*, 39–53.

Coelho, L., A. C. Soares, N. F. F. Ebecken, J. L. D. Alves, and L. Landau (2005), The impact of constitutive modeling of porous rocks on 2-D wellbore stability analysis, *J. Petrol. Sci. Eng.*, *46*, 81–100.

Curran, J. H., and M. M. Carroll (1979), Shear stress enhancement of void compaction, *J. Geophys. Res.*, *84*, 1105–1112.

Cuss, R. J., E. H. Rutter, and R. F. Holloway (2003), The application of critical state soil mechanics to the mechanical behaviour of porous sandstones, *Int. J. Rock Mech. Min. Sci.*, *40*, 847–862.

Davis, R. O., and A. P. S. Selvadurai (2002), *Plasticity and Geomechanics*, Cambridge Univ. Press, New York.

Desai, C. S., and H. J. Siriwardane (1984), *Constitutive Laws for Engineering Materials, With Emphasis on Geologic Materials*, Prentice-Hall, Upper Saddle River, N. J.

Deshpande, V. S., and N. A. Fleck (2000), Isotropic constitutive models for metallic foams, *J. Mech. Phys. Solids*, *48*, 1253–1283.

DiGiovanni, A. A., J. T. Fredrich, D. J. Holcomb, and W. A. Olsson (2000), Micromechanics of compaction in an analogue reservoir sandstone, in *Pacific Rocks 2000: Rock Around the Rim*, *Proceedings of the 4th North American Rock Mechanics Symposium, Seattle, Washington, July 31–August 3, 2000*, pp. 1153–1160, A. A. Balkema, Brookfield, Vt.

DiMaggio, F. L., and I. S. Sandler (1971), Material model for granular soils, *J. Eng. Mech. Div. Am. Soc. Civ. Eng.*, *97*, 935–950.

Drucker, D. C. (1951), A more fundamental approach to plastic stress strain relations, in *Proceedings of the 1st US National Congress Applied Mechanics*, pp. 487–491, Am. Soc. of Mech. Eng., New York.

Fisher, Q. J., M. Casey, M. B. Clennell, and R. J. Knipe (1999), Mechanical compaction of deeply buried sandstones of the North Sea, *Mar. Pet. Geol.*, *16*, 605–618.

Fossum, A. F., and J. T. Fredrich (2000), Cap plasticity models and dilatant and compactive pre-failure deformation, in *Pacific Rocks 2000: Rock Around The Rim*, *Proceedings of the 4th North American Rock Mechanics Symposium, Seattle, Washington, July 31–August 3, 2000*, pp. 1169–1176, A. A. Balkema, Brookfield, Vt.

Fredrich, J. T., and A. F. Fossum (2002), Large-scale three-dimensional geomechanical modeling of reservoirs: Examples from California and the deepwater Gulf of Mexico, *Oil Gas Sci. Technol.*, *57*, 423–441.

Grueschow, E. (2005), Yield cap constitutive models for predicting compaction localization in high porosity sandstone, Ph.D. thesis, Northwestern Univ., Evanston, Ill.

Grueschow, E., and J. W. Rudnicki (2005), Elliptic yield cap constitutive modeling for high porosity sandstone, *Int. J. Solids Struct.*, *42*, 4574–4587.

Guéguen, Y., L. Dormieux, and M. Boutéca (2004), Fundamentals of poromechanics, in *Mechanics of Fluid-Saturated Rocks*, *Int. Geophys. Ser.*,

vol. 89, edited by Y. Guéguen and M. Boutéca, pp. 1–41, Elsevier, New York.

Hamiel, Y., V. Lyakhovsky, and A. Agnon (2004), Coupled evolution of damage and porosity in poroelastic media: Theory and applications to deformation of porous rocks, *Geophys. J. Int.*, *156*, 701–713.

Handin, J., R. V. Hager, M. Friedman, and J. N. Feather (1963), Experimental deformation of sedimentary rock under confining pressure: Pore pressure effects, *AAPG Bull.*, *47*, 717–755.

Holcomb, D. J., and W. A. Olsson (2003), Compaction localization and fluid flow, *J. Geophys. Res.*, *108*(B6), 2290, doi:10.1029/2001JB000813.

Issen, K. A. (2002), The influence of constitutive models on localization conditions for porous rock, *Eng. Fract. Mech.*, *69*, 1891–1906.

Issen, K. A., and J. W. Rudnicki (2000), Conditions for compaction bands in porous rock, *J. Geophys. Res.*, *105*, 21,529–21,536.

Karner, S. L., J. S. Chester, F. M. Chester, A. K. Kronenberg, and A. J. Hajash (2005), Laboratory deformation of granular quartz sand: Implications for the burial of clastic rocks, *AAPG Bull.*, *89*, 603–625.

Klein, E., P. Baud, T. Reuschlé, and T. Wong (2001), Mechanical behaviour and failure mode of Bentheim sandstone under triaxial compression, *Phys. Chem. Earth, Part A*, *26*, 33–38.

Menéndez, B., W. Zhu, and T. Wong (1996), Micromechanics of brittle faulting and cataclastic flow in Berea sandstone, *J. Struct. Geol.*, *18*, 1–16.

Mollema, P. N., and M. A. Antonellini (1996), Compaction bands: A structural analog for anti-mode I cracks in aeolian sandstone, *Tectonophysics*, *267*, 209–228.

Nagel, N. B. (2001), Compaction and subsidence issues within the petroleum industry: From Wilmington to Ekofisk and beyond, *Phys. Chem. Earth, Part A*, *26*, 3–14.

Olsson, W. A. (1999), Theoretical and experimental investigation of compaction bands in porous rock, *J. Geophys. Res.*, *104*, 7219–7228.

Olsson, W. A., and D. J. Holcomb (2000), Compaction localization in porous rock, *Geophys. Res. Lett.*, *27*, 3537–3540.

Paterson, M. S., and T. Wong (2005), *Experimental Rock Deformation: The Brittle Field*, Springer, New York.

Ricard, Y., and D. Bercovici (2003), Two-phase damage theory and crustal rock failure: The theoretical 'void' limit, and the prediction of experimental data, *Geophys. J. Int.*, *155*, 1057–1064.

Rudnicki, J. W. (2002), Conditions for compaction and shear bands in a transversely isotropic material, *Int. J. Solids Struct.*, *39*, 3741–3756.

Rudnicki, J. W., and J. R. Rice (1975), Conditions for the localization of deformation in pressure sensitive dilatant materials, *J. Mech. Phys. Solids*, *23*, 371–394.

Schofield, A., and P. Wroth (1968), *Critical State Soil Mechanics*, 310 pp., McGraw-Hill, New York.

Sheldon, H. A., A. Barnicoat, and A. Ord (2006), Numerical modelling of faulting and fluid flow in porous rocks: An approach based on critical state soil mechanics, *J. Struct. Geol.*, *28*, 1468–1482.

Sibson, R. H. (1994), Crustal stress, faulting and fluid flow, in *Geofluids, Origin, Migration and Evolution of Fluids in Sedimentary Basins*, edited by J. Parnell, *Geol. Soc. Spec. Publ.*, *78*, 69–84.

Sternlof, K. R., J. R. Chapin, D. D. Pollard, and L. J. Durlofsky (2004), Permeability effects of deformation band arrays in sandstone, *AAPG Bull.*, *88*, 1–15.

Tembe, S., V. Vajdova, P. Baud, W. Zhu, and T. Wong (2005), Compactive yield behavior of two porous sandstones under undrained conditions, *Mech. Mater.*, in press.

Tembe, S., V. Vajdova, T. Wong, and W. Zhu (2006), Initiation and propagation of strain localization in circumferentially notched samples of two porous sandstones, *J. Geophys. Res.*, *111*, B02409, doi:10.1029/2005JB003611.

Vajdova, V., T. Wong, D. E. Farrell, V. Challa, and K. A. Issen (2003), Experimental observation and numerical simulation of initiation and propagation of compaction band in sandstone, paper presented at 16th ASCE Engineering Mechanics Conference, Seattle, Wash.

Vajdova, V., P. Baud, and T. Wong (2004a), Permeability evolution during localized deformation in Bentheim sandstone, *J. Geophys. Res.*, *109*, B10406, doi:10.1029/2003JB002942.

Vajdova, V., P. Baud, and T. Wong (2004b), Compaction, dilatancy and failure in porous carbonate rocks, *J. Geophys. Res.*, *109*, B05204, doi:10.1029/2003JB002508.

Wong, T., and P. Baud (1999), Mechanical compaction of porous sandstone, *Oil Gas Sci. Technol.*, *54*, 715–727.

Wong, T., H. Szeto, and J. Zhang (1992), Effect of loading path and porosity on the failure mode of porous rocks, *Appl. Mech. Rev.*, *45*, 281–293.

Wong, T., C. David, and W. Zhu (1997), The transition from brittle faulting to cataclastic flow in porous sandstones: Mechanical deformation, *J. Geophys. Res.*, *102*, 3009–3025.

Wong, T., P. Baud, and E. Klein (2001), Localized failure modes in a compactant porous rock, *Geophys. Res. Lett.*, *28*, 2521–2524.

Wood, D. M. (1990), *Soil Behavior and Critical State Soil Mechanics*, 462 pp., Cambridge Univ. Press, New York.

Wu, C.-Y., O. M. Ruddy, A. C. Bentham, B. C. Hancock, S. M. Best, and J. A. Elliott (2005), Modelling the mechanical behaviour of pharmaceutical powders during compaction, *Powder Technol.*, *152*, 107–117.

Wu, X. Y., P. Baud, and T. Wong (2000), Micromechanics of compressive failure and spatial evolution of anisotropic damage in Darley Dale sandstone, *Int. J. Rock Mech. Min. Sci.*, *37*, 143–160.

Zeuch, D. H., J. M. Grazier, J. G. Argüello, and K. G. Ewsuk (2001), Mechanical properties and shear failure surfaces for two alumina powders in triaxial compression, *J. Mater. Sci.*, *36*, 2911–2924.

Zhang, J., T. Wong, and D. M. Davis (1990a), Micromechanics of pressure-induced grain crushing in porous rocks, *J. Geophys. Res.*, *95*, 341–352.

Zhang, J., T. Wong, T. Yanagidani, and D. M. Davis (1990b), Pressure-induced microcracking and grain crushing in porous rocks in Boise and Berea sandstones: Acoustic emission and quantitative microscopy measurements, *Mech. Mater.*, *9*, 1–15.

P. Baud, Institut de Physique du Globe, Ecole et Observatoire des Sciences de la Terre (CNRS/ULP), 5 rue Rene Descartes, F-67084 Strasbourg, France. (pbaud@east.u-strasbg.fr)

V. Vajdova, ReedHycalog, A Grant Prideco Company, 6501 Navigation Blvd., Houston, TX 77011, USA.

T.-f. Wong, Department of Geosciences, State University of New York at Stony Brook, Stony Brook, NY 11794-2100, USA.